Uncertainty quantification for the modal shape sensing of structures undergoing geometrically non-linear deformation

Gundlach, Janto; Böswald, Marc; Sodja, Jurij

DOI
10.1016/j.ymssp.2025.113249

Publication date
2025

Document Version
Final published version

Published in
Mechanical Systems and Signal Processing

Citation (APA)
Gundlach, J., Böswald, M., & Sodja, J. (2025). Uncertainty quantification for the modal shape sensing of structures undergoing geometrically non-linear deformation. *Mechanical Systems and Signal Processing*, *239*, Article 113249. https://doi.org/10.1016/j.ymssp.2025.113249

Mechanical Systems and Signal Processing 239 (2025) 113249

Contents lists available at ScienceDirect

Mechanical Systems and Signal Processing

journal homepage: www.elsevier.com/locate/ymssp

Full length article

Uncertainty quantification for the modal shape sensing of structures undergoing geometrically non-linear deformation

Janto Gundlach [a,b,*], Marc Böswald [a], Jurij Sodja [b]

[a] German Aerospace Center, Institute of Aeroelasticity, Bunsenstraße 10, 37073, Göttingen, Germany
[b] Delft University of Technology, Kluyverweg 1, 2629HS, Delft, The Netherlands

ARTICLE INFO

Communicated by D. Moens

Keywords:
Shape sensing
Modal approach
Uncertainty quantification
Geometric non-linearity
High-aspect-ratio wing

ABSTRACT

Shape sensing techniques allow for the time-efficient reconstruction of displacements based on measured strain data. There are technical applications, where the structure of interest is deformed in the geometrically non-linear domain. In aeronautics, this is the case for high-aspect-ratio wings, which are more frequently found in future designs. Only shape sensing methods that specifically take the non-linearity into account, can deliver appropriate displacement estimates for such application. A shape sensing method based on the linear modal approach can be utilised incrementally to capture the geometric non-linearity; it has therefore been denoted incremental modal method (IMM). This paper presents analytical relations for the uncertainty propagation for the various input quantities of the method, specifically strain mode shapes, displacement mode shapes, and measured strain. Deterministic shape sensing and uncertainty propagation are demonstrated using data obtained with a finite element model of a high-aspect-ratio wing experiencing geometric non-linear deflections in flapwise bending. Virtual strain and acceleration sensors are assumed for this setup, imitating the instrumentation conceivable for experimental work. The results obtained by analytical propagation are compared to Monte Carlo simulations for the purpose of validation. The derived propagation formulas make it possible to follow the evolution of the uncertainties over the number of increments. Given that the variability of the input quantities is known, the number of increments that minimise uncertainties can be determined for a model-free application of the shape sensing. Together with the deterministic estimates provided by an FE model, it is possible to determine the ideal number of increments for a specific shape sensing application in the geometrically non-linear domain.

1. Introduction

Shape sensing methods, which allow for the reconstruction of displacements from measured strain data, have received greater attention in the literature over the last three decades [1]. Research in this field has primarily focused on linear problems, with three reconstruction principles being the most widely documented: methods leveraging the kinematics of structural elements, in particular beams [2,3], methods that minimise error functionals within the inverse finite element (iFEM) framework [1,4], and techniques employing the linear superposition of basis functions, for example displacement mode shapes, to reconstruct displacements [5–7].

When applied to problems involving large deformations, in terms of significant displacements and rotations, the results of the above methods are subject to systematic errors. On that account, more recent work which is specifically aimed to reconstruct the

* Corresponding author at: German Aerospace Center, Institute of Aeroelasticity, Bunsenstraße 10, 37073, Göttingen, Germany.
E-mail address: janto.gundlach@dlr.de (J. Gundlach).

https://doi.org/10.1016/j.ymssp.2025.113249
Received 10 March 2025; Received in revised form 25 June 2025; Accepted 20 August 2025
Available online 17 September 2025

displacement of wing structures in the geometrically non-linear range has been presented. The Modal Rotation Method (MRM), introduced in [8], relies on mode shapes defined through curvatures rather than displacements. These curvature shapes are built in segments from modal rotations which are obtained from a normal modes analysis of a finite element model. This allows for a linearised assessment of the change in bending slope for each segment and their summation across the entire structure, utilising nonlinear kinematics. MRM has successfully been applied on data measured in experiments with the Pazy wing [9]. Subsequently, the deflection estimates have been employed in flutter calculations to assess the dynamic stability of the wing in the non-linear static deformation state. Two other approaches are suggested in [10] to deal with non-linear deflections: an integration-based two-step method for optical fibres is presented relying on beam kinematics (cf. [11]), where local rotations are considered in the deformation computation and compared to results obtained with superposed non-linear deflection curves serving as basis functions. The basis functions are calculated in static non-linear FE simulations of a rectangular high-aspect-ratio wing. In [12,13] it is described how iFEM can be applied in an iterative algorithm to reconstruct the displacement field of plates undergoing large deflections. Therefore, the strain data must be evaluated at each load increment to obtain the corresponding iFEM displacement estimate. Using the displacements, the geometry is updated and the (virtual) strain sensor orientation is adjusted. This procedure is repeated until the overall deformation shape is obtained.

There are applications in which modal parameters of the structure are continuously recorded experimentally. These include wind tunnel tests at the flutter boundary of wing models [14] and aircraft flight vibration tests [15,16], but also bridges that undergo permanent monitoring [17]. If the deflection of the structure at distributed locations is of interest in such applications, the linear superposition of identified mode shapes, serving as basis functions, is a conceivable method. Test scenarios involving geometrically non-linear deformation are particularly interesting for this shape sensing approach, because the modal parameters and thus mode shapes change with deflection. In [18], an incremental modal method (IMM) is introduced that leverages the change of mode shapes and adopts the idea of [12,13] to approach the total deflection in the geometrically non-linear regime in linearised steps. In the process, different deformation states corresponding to various test points can be utilised to determine large displacements. The suggested procedure has been applied on data obtained by non-linear finite element simulation of a tapered and swept high-aspect-ratio wing and compared to results estimated with MRM. If the method is provided with identified modes, it represents a model-free shape sensing technique.

The present article aims to build upon this research by providing a more detailed explanation of the method and applying it to reconstruct the bending and torsional deflections using strain and accelerometer instrumentation suitable for a wind tunnel test. Furthermore, for the first time, the behaviour of the incremental approach is investigated with respect to uncertainties of the input quantities. In laboratory experiments and in real applications, modal parameters are commonly identified using experimental or operational modal analysis methods [19,20], which are also applicable to strain signals to obtain strain mode shapes [21–23]. Experimentally determined mode shapes inevitably exhibit variability due to different environmental conditions, instrumentation inaccuracies, measurement noise, and scatter caused by different identification techniques. The measured strains are also subject to uncertainties. In this paper, the effects of uncertainties in these input quantities of IMM are investigated. In the process, it is assumed that the measured strains as well as the strain and displacement mode shapes of the different deformation states are not subject to systematic bias, but deviate randomly from the true value. The impact of these uncertainties on the estimated displacements is determined using Gaussian error propagation based on the standard deviations of the input parameters. It becomes evident how uncertainties in the measured strains and mode shapes impact the accuracy of the displacement estimation. This represents valuable insight of the procedure with regard to the application in a real test scenario.

The rest of the paper is structured as follows. Section 2 of this paper describes the modal shape sensing method used for displacement estimation. Furthermore, the methodology of uncertainty propagation is elucidated. Since the target application is high-aspect-ratio wings, the case of application is a finite element model of such a wing. A deterministic reference solution from an FE model is necessary to evaluate the accuracy of the method in combination with output uncertainties. The model of the high-aspect-ratio wing and its virtual instrumentation is described in Section 3; the deterministic shape sensing results which are not affected by uncertainties are presented there as well. The results of the uncertainty analysis and their implication for test application are reported in Section 4. Finally, the main findings of this investigation are concluded in Section 5.

2. Modal shape sensing method for large displacements

Among the shape sensing methods that rely on strain measurements, the incremental procedure proposed here utilises the modal approach. If only a single increment is used, the method resembles to the suggested techniques described in [5,7], which are applicable to linear problems.

2.1. Modal method for linear problems

According to the modal approach, the displacement estimates can directly be derived from the linear superposition of displacement mode shapes with modal coordinates being the weightings in the linear combination. In the process, the structure is represented as a system with N degrees of freedom, either obtained through finite element discretisation or defined by the measurement degrees of freedom in modal testing. The displacement expressed in terms of the modal approach reads:

$$\boldsymbol{u}(t) = \sum_{m=1}^{N} \boldsymbol{\phi}_m q_m(t) = \boldsymbol{\Phi}\boldsymbol{q}(t). \tag{1}$$

$\boldsymbol{\Phi}$ contains the mode shapes $\boldsymbol{\phi}_m$ in columns and is commonly denoted as modal matrix, and $\boldsymbol{q}$ is a vector of time-dependent modal coordinates q_m, indicating the quantitative participation of each mode in the overall deformation. Similarly, the strain at selected positions can also be expressed by a corresponding linear combination:

$$\boldsymbol{\varepsilon}(t) = \sum_{m=1}^{N} \boldsymbol{\psi}_m q_m(t) = \boldsymbol{\Psi}\boldsymbol{q}(t), \tag{2}$$

where $\boldsymbol{\Psi}$ represents likewise the strain modal matrix. When both modal matrices are obtained from an FE model, the strain mode shapes are derived kinematically from the displacement field. Consequently, each FE node contains both displacement and strain mode shape components. However, in a model-free approach, i.e., when based on experimentally identified modes, displacement and strain mode shape components are typically available only at different positions determined by the instrumentation. Also, the number of accelerometers N_u is commonly different from the number of strain sensors N_ε. As the components of $\boldsymbol{\varepsilon}$ are measured during the application of the shape sensing, at least the strain mode shape components of these strain sensor positions must be provided. In many applications, the maximum number of modes considered in the linear combination is limited by the number of strain sensors employed during the test, as $N_\varepsilon < N_u$, which determines how many modes can be distinguished with the chosen strain sensor distribution [5,24].

When both displacement and strain modes are determined from finite elements, they correspond to the same scaling. For modes identified from measured data, a consistent scaling must be enforced (cf. [21]) to ensure the uniqueness of the modal coordinates. Only then the displacement estimate from measured strain can be computed via

$$\hat{\boldsymbol{u}}(t) = \boldsymbol{\Phi}\boldsymbol{\Psi}^{\dagger}\boldsymbol{\varepsilon}(t) = \boldsymbol{T}\boldsymbol{\varepsilon}(t). \tag{3}$$

The pseudo-inverse $\boldsymbol{\Psi}^{\dagger}$ of the strain modal matrix in combination with the displacement modal matrix can be summarised in a matrix $\boldsymbol{T} = \boldsymbol{\Phi}\boldsymbol{\Psi}^{\dagger}$, often referred to as displacement-strain-transformation (DST) matrix [25,26], which defines the linear mapping from strain to displacement. In view of Eq. (3), the spatial resolution of the displacement estimate depends on the dimension of the displacement mode shape vectors. Their size depends on either the nodal degrees of freedom from FE discretisation or the number of the measurement degrees of freedom in modal testing.

In the framework of a hybrid approach, the modal matrices forming the basis of the DST matrix can also be a combination of test results and FE analysis [27]. Since FE models can be flawed and might require updating using test data [28], it is assumed that experimentally determined mode shapes are generally preferable, having a positive effect on the accuracy of displacement estimation.

2.2. Incremental modal method for non-linear problems

Modal parameters, such as mode shapes, characterise the dynamic properties of structural systems. When a wing structure is exposed to external forces undergoing large deformations, these system properties are subjected to changes [18]. Consequently, in the geometrically non-linear domain, the DST matrix evolves with deformation as $\boldsymbol{T} = \boldsymbol{T}(\boldsymbol{u})$, since both displacement and strain mode shapes are modified. It is thus important to realise that the mode shapes of the undeformed structure can only be used for the shape sensing of small deformations where the assumption of linearity still holds.

The solution strategy proposed here for the shape sensing of large deformation is to account for changes of the modes in an incremental sense between different deformation states. In this approach, modes are determined for each deformation state and used solely to estimate displacements after a strain increment $\boldsymbol{\Delta\varepsilon}$, provided that the increment is sufficiently small for linearity to remain valid. This concept is illustrated in Fig. 1 for a reference line of a deformed structure which is clamped at the root. The superscripts indicate quantities of the ith increment of the overall deformation. $\boldsymbol{T}^0$ thus defines the DST of the undeformed structure, which can be used for displacement reconstruction of linear problems, while $\boldsymbol{T}^{i-1}$ represents the appropriate modal basis for a given deformation state before the transition to the ith increment.

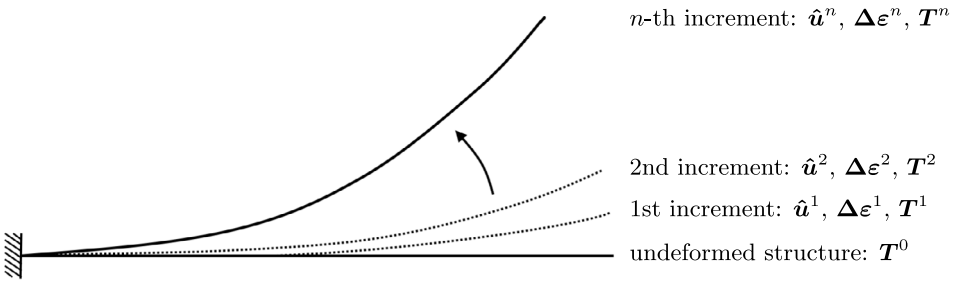

Fig. 1. Schematic of incremental modal method (IMM).

Given that sufficient increments are available where modes are determined, a displacement estimate in the geometrically non-linear range is obtained by summation of the displacement increments. For a reconstruction over n increments, the final shape sensing result can be computed with

$$\begin{aligned}\hat{\boldsymbol{u}}^1 &= \boldsymbol{T}^0\boldsymbol{\varepsilon}^1\\ \hat{\boldsymbol{u}}^2 &= \hat{\boldsymbol{u}}^1 + \boldsymbol{T}^1(\boldsymbol{\varepsilon}^2 - \boldsymbol{\varepsilon}^1) = \hat{\boldsymbol{u}}^1 + \boldsymbol{T}^1\boldsymbol{\Delta\varepsilon}^2 = \hat{\boldsymbol{u}}^1 + \boldsymbol{\Delta\hat{u}}^2\\ &\vdots\\ \hat{\boldsymbol{u}}^n &= \hat{\boldsymbol{u}}^{n-1} + \boldsymbol{T}^{n-1}\boldsymbol{\Delta\varepsilon}^n = \hat{\boldsymbol{u}}^{n-1} + \boldsymbol{\Delta\hat{u}}^n.\end{aligned} \tag{4}$$

As seen from the expressions, the measured total strain for each increment $\boldsymbol{\varepsilon}^i$ is not employed, but only the strain increments $\boldsymbol{\Delta\varepsilon}^i = \boldsymbol{\varepsilon}^i - \boldsymbol{\varepsilon}^{i-1}$ between deformation states. At each step, the overall displacement is updated by an increment

$$\boldsymbol{\Delta\hat{u}}^i = \boldsymbol{T}^{i-1}\boldsymbol{\Delta\varepsilon}^i. \tag{5}$$

Using a strain-free initial condition, i.e. $\boldsymbol{\varepsilon}^1 = \boldsymbol{\Delta\varepsilon}^1$, the displacement estimate in Eq. (4) can be computed as a summation of DSTs and strain increments over different states of deformation:

$$\hat{\boldsymbol{u}}^n = \sum_{i=1}^{n} \boldsymbol{T}^{i-1}\boldsymbol{\Delta\varepsilon}^i. \tag{6}$$

It is worth emphasising that IMM is not limited to applications on slender structures. In principle, the approach can be used for structures of any shape that undergo geometrically non-linear deformations.

When applying the incremental modal method, the choice of the number and size of increments is problem-specific. Even though the method is intended as a model-free technique, i.e., based solely on experimental mode shapes identified during testing, the availability of an FE model is beneficial for effective test planning. In general, geometric non-linearity can be captured more accurately by increasing the number of increments. As demonstrated in Section 3 using the model of a high-aspect-ratio wing, non-linear static finite element simulations can assist in determining the number of increments required to achieve a desired level of accuracy. Furthermore, Section 4.2 describes how combining deterministic FE results with known displacement uncertainties supports decision-making regarding an appropriate number of increments for evaluating Eq. (6).

Apart from aspects related to geometric non-linearity, all principles relevant to conventional modal shape sensing for linear problems (cf. Eq. (3)) remain applicable. In particular, an FE model is useful for evaluating sensor placement. For instance, the separation of mode shapes can be quantified using the modal assurance criterion (MAC, [29]). Mutually distinguishable mode shapes, indicated by low pairwise MAC values, reflect a high degree of linear independence. This, in turn, results in well-conditioned modal matrices $\boldsymbol{\Phi}$ and $\boldsymbol{\Psi}$, which enhance the stability and accuracy of the strain-to-displacement transformation. IMM could also be applied based on FE mode shapes extracted from deformed states (cf. Section 3), or in a hybrid manner following the approach in [27].

Nevertheless, one of the key advantages of the incremental modal method lies in its model-free nature. Experimentally identified mode shapes can, in many cases, lead to higher accuracy than their numerical counterparts, as they inherently reflect real boundary conditions, structural imperfections, and operational variability. This makes IMM particularly suitable for in-situ applications, where the relevant mode shapes of the deformed structure are assumed to be continuously identified during operation (cf. [14–16]), and local strain measurements are available in parallel. The ability to work without relying on an FE model not only enhances flexibility but also avoids modelling uncertainties, which can otherwise lead to inaccurate shape sensing results. Accordingly, the present investigation focuses on how the incremental application of the method influences the propagation of uncertainties arising from experimentally determined input parameters, as discussed in the following.

2.3. Propagation of uncertainties through load increments

Applying the incremental reconstruction method, uncertainties have an impact on each individual estimate at different deformation increments. To address this, the uncertainties from previous load steps must be propagated throughout the full deformation history. In this context, the uncertainties of the different input quantities of the shape sensing algorithm, i.e., the measured strain and the strain and displacement modal matrices, respectively, are assumed to be uncorrelated and normally distributed.

2.3.1. Uncertainties arising from measured strain

In order to assess possible deviation from a mean or expected value of the shape sensing estimate, it is assumed that each strain sensor is considered to record a signal with the same level of variability. The magnitude of the variability is defined by setting a standard deviation σ_ε to a threshold value in microstrain, which aligns with the general observation that sensors with a stronger signal exhibit a better signal-to-noise ratio. σ_ε reflects random measurement noise, typically originating from analog-to-digital conversion or the inherent noise of strain gauge amplifiers. This type of noise is generally well approximated by a normal distribution.

Assuming that the identification of strain mode shapes is independent from instantaneous strain measurements, the mapping to displacement is linear in strain. Consequently, normally distributed strain input results in normally distributed components of the approximated displacement vector. According to Eq. (5), displacement degree of freedom j of the ith increment is computed with

$$\begin{aligned}\Delta\hat{u}_j^i &= T_{j1}^{i-1}\Delta\varepsilon_1^i + \cdots + T_{jN_\varepsilon}^{i-1}\Delta\varepsilon_{N_\varepsilon}^i\\ &= \sum_{k=1}^{N_\varepsilon} T_{jk}^{i-1}\Delta\varepsilon_k^i, \quad j = 1, \ldots, N_u.\end{aligned} \tag{7}$$

Furthermore, assuming that the uncertainty among strain sensors is uncorrelated, its impact on the displacement estimates can be evaluated using Gaussian uncertainty propagation [30]. Irrespective of whether for strain increments $\Delta\varepsilon_k^i$ or the total strain ε_k^i in a deformed state, each strain channel is expected to exhibit the same measurement uncertainty defined by $\sigma_{\Delta\varepsilon_k^i} = \sigma_\varepsilon$. Taking into account that the coefficients from the DST matrix are the sensitivities of the error propagation, one can obtain the standard deviation of the output displacement as a consequence of variable strain input:

$$\begin{aligned}\sigma^{\varepsilon}_{\Delta\hat{u}_j^i} &= \sqrt{\left(\frac{\partial\Delta u_j^i}{\partial\Delta\varepsilon_1^i}\sigma_{\Delta\varepsilon_1^i}\right)^2 + \cdots + \left(\frac{\partial\Delta u_j^i}{\partial\Delta\varepsilon_{N_\varepsilon}^i}\sigma_{\Delta\varepsilon_{N_\varepsilon}^i}\right)^2} \\ &= \sigma_\varepsilon\sqrt{\sum_{k=1}^{N_\varepsilon}\left(T_{jk}^{i-1}\right)^2}.\end{aligned} \tag{8}$$

The displacement increments are calculated independently for each step and added up to the total displacement estimate (cf. Eq. (6)). For this reason, the resulting uncertainty from consecutive increments can be calculated using the sum rule of variances [31]. On the other hand, the sensitivities expressed by the DST matrix components T_{jk}, change in every increment due to the change of the mode shapes during deformation. Hence, the variance of all displacement estimates after n increments can be computed as

$$\begin{aligned}\left(\sigma^{\varepsilon}_{\hat{u}_j^n}\right)^2 &= \sum_{i=1}^{n}\left(\sigma^{\varepsilon}_{\Delta\hat{u}_j^i}\right)^2 \\ &= \sigma_\varepsilon^2\sum_{i=1}^{n}\sum_{k=1}^{N_\varepsilon}\left(T_{jk}^{i-1}\right)^2,\end{aligned} \tag{9}$$

such that the final uncertainty in the displacement estimate expressed by the standard deviation reads

$$\sigma^{\varepsilon}_{\hat{u}_j^n} = \sigma_\varepsilon\sqrt{\sum_{i=1}^{n}\sum_{k=1}^{N_\varepsilon}\left(T_{jk}^{i-1}\right)^2}. \tag{10}$$

From Eq. (10) it becomes apparent that the uncertainty of the final estimate at each displacement degree of freedom scales linearly with the strain input uncertainty σ_ε. Without additional knowledge of T_{jk}^{i-1}, which varies across increments and is strongly influenced by the number and placement of strain sensors, the relationship between the uncertainties and the number of increments remains unclear. However, assuming that only minor changes occur in the DST matrix during deformation and for a fixed number of strain sensors, one observes:

$$\sigma^{\varepsilon}_{\hat{u}_j^n} \propto \sqrt{n}, \tag{11}$$

indicating that the output uncertainty increases proportionally to the square root of the total number of increments n. Although a low number of increments results in lower uncertainties, it is important to note that the accuracy of the results can be compromised, if the geometric non-linearity is not adequately captured.

2.3.2. *Uncertainty arising from displacement mode shapes*

As displacement mode shapes must be identified in every considered state of deformation, uncertainties in the modal identification process also have an impact on each increment. To investigate the effects of mode shape variability, the coefficients of the DST matrices are expressed as a function of mode shape components as

$$T_{jk}^{i-1} = \sum_{m=1}^{N_m}\boldsymbol{\Phi}_{jm}^{i-1}\boldsymbol{\Psi}_{mk}^{\dagger,i-1}. \tag{12}$$

The number of mode shapes N_m considered in the mapping is arbitrary, for instance: $N_m = \min(N_u, N_\varepsilon)$. To simplify the following derivation, the order of the summation over $\boldsymbol{\Psi}_{mk}^{\dagger,i-1}$ can be commuted such that Eq. (7) is rearranged to

$$\begin{aligned}\Delta\hat{u}_j^i &= \sum_{k=1}^{N_\varepsilon}\left(\sum_{m=1}^{N_m}\boldsymbol{\Phi}_{jm}^{i-1}\boldsymbol{\Psi}_{mk}^{\dagger,i-1}\right)\Delta\varepsilon_k^i \\ &= \sum_{m=1}^{N_m}\boldsymbol{\Phi}_{jm}^{i-1}\left(\sum_{k=1}^{N_\varepsilon}\boldsymbol{\Psi}_{mk}^{\dagger,i-1}\Delta\varepsilon_k^i\right).\end{aligned} \tag{13}$$

The propagation of uncertainty in displacement mode shapes requires the computation of displacement sensitivities with respect to individual mode shape components. These are defined by

$$\frac{\partial\Delta\hat{u}_j^i}{\partial\boldsymbol{\Phi}_{jm}^{i-1}} = \sum_{k=1}^{N_\varepsilon}\boldsymbol{\Psi}_{mk}^{\dagger,i-1}\Delta\varepsilon_k^i, \tag{14}$$

and employing the Gaussian propagation formula one can obtain the standard deviation of the output displacement as a consequence of variability in the displacement mode shapes with

$$\sigma^{\boldsymbol{\Phi}}_{\Delta\hat{u}^i_j} = \sqrt{\sum_{m=1}^{N_m}\left(\left(\sum_{k=1}^{N_\varepsilon}\boldsymbol{\Psi}^{\dagger,i-1}_{mk}\Delta\varepsilon^i_k\right)^2\sigma^2_{\boldsymbol{\Phi}^{i-1}_{jm}}\right)}. \tag{15}$$

In contrast to the uncertainty in the strain measurements, $\sigma_{\boldsymbol{\Phi}^{i-1}_{jm}}$ is not considered to be the same value for each mode shape component and for each mode; it is rather scaled to the mean values of the mode shape component, which is the respective FE mode shape component in the case exemplified in Section 3. The scaling is accomplished with a unique scalar that can be understood as a coefficient of variation:

$$c^{\boldsymbol{\Phi}}_v = \frac{\sigma_{\boldsymbol{\Phi}^{i-1}_{jm}}}{\boldsymbol{\Phi}^{i-1}_{jm}}. \tag{16}$$

From this definition, using again the sum rule of variances (cf. Eq. (9)), the standard deviation after n consecutive increments follows with:

$$\sigma^{\boldsymbol{\Phi}}_{\hat{u}^n_j} = c^{\boldsymbol{\Phi}}_v\sqrt{\sum_{i=1}^{n}\sum_{m=1}^{N_m}\left(\left(\sum_{k=1}^{N_\varepsilon}\boldsymbol{\Psi}^{\dagger,i-1}_{mk}\Delta\varepsilon^i_k\right)^2\boldsymbol{\Phi}^{i-1\,2}_{jm}\right)}. \tag{17}$$

The assumptions underlying Eq. (17) have already been introduced above, but are reiterated here for clarity. The formulation assumes that the uncertainty in the displacement mode shapes is uncorrelated, normally distributed, and scales with the respective mean values according to the coefficient of variation defined in Eq. (16). Furthermore, according to IMM, the mapping from strain to displacement is assumed to be linear within each increment. These assumptions enable the application of the Gaussian error propagation formula and the summation of variances across increments.

The resulting standard deviation relates linearly with the coefficient of variation for the displacement mode shape components. For a higher number of increments to reach a specific non-linear state of deformation, the increment size is reduced, meaning that $\Delta\varepsilon^i_k \sim \frac{1}{n}$. As a consequence, assuming again small changes of strain mode shapes and displacement mode shapes, and a fixed number of modes and strain sensors, the dependency to the number of increments reads

$$\sigma^{\boldsymbol{\Phi}}_{\hat{u}^n_j} \propto \frac{1}{\sqrt{n}}, \tag{18}$$

indicating a decreasing output uncertainty if the source is to be found in the displacement mode shapes.

2.3.3. Uncertainty arising from strain mode shapes

As the displacement sensitivities with respect to every strain component of the strain modal matrix must be computed, the propagation formula accounting for these uncertainties reads

$$\sigma^{\boldsymbol{\Psi}}_{\Delta\hat{u}^i_j} = \sqrt{\sum_{a=1}^{N_\varepsilon}\sum_{b=1}^{N_m}\left(\frac{\partial\Delta\hat{u}^i_j}{\partial\boldsymbol{\Psi}^{i-1}_{ab}}\sigma_{\boldsymbol{\Psi}^{i-1}_{ab}}\right)^2}. \tag{19}$$

Unlike the other input quantities, there is a non-linear relationship between the elements of $\boldsymbol{\Psi}$ and the shape sensing estimates; Eq. (19) represents only an approximation of the output uncertainty if the linearised Gaussian propagation law is applied. In view of Eq. (13), one finds that every component of $\boldsymbol{\Psi}^\dagger$ has to be considered for calculation of the partial derivatives with respect to $\boldsymbol{\Psi}^{i-1}_{ab}$. The matrix containing these derivatives can be derived by definition of the Moore–Penrose pseudoinverse. Derivation with respect to an individual component of the strain modal matrix leads to

$$\frac{\partial\boldsymbol{\Psi}^\dagger}{\partial\boldsymbol{\Psi}_{ab}} = -\left(\boldsymbol{\Psi}^T\boldsymbol{\Psi}\right)^{-1}\left(\boldsymbol{E}^T\boldsymbol{\Psi}+\boldsymbol{\Psi}^T\boldsymbol{E}\right)\left(\boldsymbol{\Psi}^T\boldsymbol{\Psi}\right)^{-1}\boldsymbol{\Psi}^T + \left(\boldsymbol{\Psi}^T\boldsymbol{\Psi}\right)^{-1}\boldsymbol{E}^T, \tag{20}$$

where $\boldsymbol{E}$ equals one at E_{ab} and zero otherwise. The partial derivatives in Eq. (19) rely on the analytical expression for the sensitivity of the pseudoinverse with respect to perturbations in the original strain modal matrix, as shown in Eq. (20). This expression assumes that $\boldsymbol{\Psi}^T\boldsymbol{\Psi}$ is invertible and that uncertainties in $\boldsymbol{\Psi}$ are sufficiently small for a first-order approximation to remain valid. The derivation neglects any higher-order terms and is therefore most accurate when the strain mode shapes vary slightly around their nominal values.

By defining $\boldsymbol{\Gamma} = \left(\boldsymbol{\Psi}^T\boldsymbol{\Psi}\right)^{-1}$, derivatives of the pseudo inverse components can be computed as

$$\frac{\partial\boldsymbol{\Psi}^\dagger_{mk}}{\partial\boldsymbol{\Psi}_{ab}} = \Gamma_{mb}\left(\delta_{ka} - \sum_{r=1}^{N_m}\sum_{s=1}^{N_m}\Gamma_{rs}\boldsymbol{\Psi}_{ks}\boldsymbol{\Psi}_{ar}\right) - \sum_{r=1}^{N_m}\sum_{s=1}^{N_m}\Gamma_{mr}\boldsymbol{\Psi}_{ar}\Gamma_{bs}\boldsymbol{\Psi}_{ks} \tag{21}$$

and employed in the expressions of the sensitivities. δ_{ka} denotes the Kronecker delta in above expression. Analogue to the displacement mode shapes, a coefficient of variation is introduced

$$c^{\boldsymbol{\Psi}}_v = \frac{\sigma_{\boldsymbol{\Psi}^{i-1}_{ab}}}{\boldsymbol{\Psi}^{i-1}_{ab}}, \tag{22}$$

which describes the variability in strain modes with respect to mean strain mode components. As c_v^{Ψ} is independent from the indices of the summation in Eq. (19) and constant for any increment, the uncertainty of the jth displacement estimate caused by variable strain mode shapes is obtained by insertion of Eqs. (21) and (22) in Eq. (19), and the application of the sum rule of variances:

$$\sigma_{u_j^n}^{\Psi} = c_v^{\Psi} \left\{ \sum_{i=1}^{n} \sum_{a=1}^{N_\varepsilon} \sum_{b=1}^{N_m} \left[\sum_{m=1}^{N_m} \Phi_{jm}^{i-1} \left(\sum_{k=1}^{N_\varepsilon} \left(\Gamma_{mb}^{i-1} \left(\delta_{ka} - \sum_{r=1}^{N_m} \sum_{s=1}^{N_m} \Gamma_{rs}^{i-1} \Psi_{ks}^{i-1} \Psi_{ar}^{i-1} \right) \right. \right. \right. \right. \\ \left. \left. \left. \left. - \sum_{r=1}^{N_m} \sum_{s=1}^{N_m} \Gamma_{mr}^{i-1} \Psi_{ar}^{i-1} \Gamma_{bs}^{i-1} \Psi_{ks}^{i-1} \right) \Delta\varepsilon_k^i \right) \Psi_{ab}^{i-1} \right]^2 \right\}^{\frac{1}{2}}. \tag{23}$$

For a fixed strain sensor setup using a constant number of modes in the shape sensing, the following dependence on the number of increments can again be established:

$$\sigma_{u_j^n}^{\Psi} \propto \frac{1}{\sqrt{n}}. \tag{24}$$

Unlike the uncertainties arising from strain measurements, the uncertainty due to variability in the modes decreases with an increasing number of increments, generally leading to higher accuracy of the method. However, it must be taken into account that the number of increments cannot be increased indefinitely in practical applications.

3. Reference deformation reconstruction

In order to assess the impact of output uncertainties on IMM estimates, a reference solution is required that would correspond to the arithmetic mean solution if the shape sensing was repeated multiple times in a test scenario. For this reason, IMM is applied to the FE model of a high-aspect-ratio wing with symmetric NACA 0012 airfoil profile [32] in the absence of uncertainties. The following section outlines the properties of the model, the simulation setup, and the virtual sensor instrumentation used for shape sensing.

3.1. Wing model and virtual instrumentation

The wing model is chosen since it features all the relevant properties of realistic wing structures. This includes a swept and tapered design, which typically reduces the accuracy of shape sensing methods compared to simpler laboratory structures such as straight beams and flat plates. In Table 1, the geometric dimensions are summarised. The FE discretisation of the model comprises shells and shear webs constructed from sandwich-structured composites, along with ribs that reinforce the cross-sections at regular intervals. The model consists of 8948 elements, primarily 4-noded shell quadrilaterals, with composite properties defined by the laminate lay-up. The FE model was developed using the DLR-AE in-house parametric model generator ModGen [33] in MSC.NASTRAN. A top-down view of the mesh is depicted in Fig. 2. As the laboratory wing is designed for multipurpose use, the model includes a folding wing tip, which is not relevant to this research. The hinge for the folding wing tip appears as a gap with 0.1 m width located at two-thirds of the wing span. For the purposes of shape sensing analysis, the hinge is blocked and modelled using RBE2 elements. The hinge midpoint is rigidly connected to the surface nodes of the neighbouring cross-sections. Due to this modelling, the region containing the hinge performs a rigid body motion and does not allow for additional deformation within this section.

The mesh indicates the position of virtual strain sensors being used both for the representation of strain modes and the strain information for calculating displacement increments according to Eq. (5). Strain is assessed in five cross-sections on the shell panels beginning at $y = 0.75$ m with equidistant spacing of $\Delta y = 1$ m in-between. The orientation of the computed strain corresponds to the first axis of the local element coordinate systems, which point in the direction of the dashed lines indicated in Fig. 2. Both the pressure and suction side of the wing are instrumented at locations symmetric to the xy-plane. In total, strain data of 20 virtual strain channels are thus available for the shape sensing; the present distribution of strain sensors is suitable to be employed to evaluate bending moments as part of a load monitoring of the wing [34]. It is assumed that accelerometers are placed equidistantly with $y = 0.5$ m at the leading and trailing edge of the wing. They enable the identification of displacement modes. Having 22 positions occupied with triaxial sensors, the mode shapes are represented by the finite element model with 66 degrees of freedom in global coordinates which serve as input for the shape sensing.

The shape sensing method presented in Section 2 is applied to a geometrically non-linear deformation state of the wing. The reference displacement field is determined by means of a NASTRAN SOL400 non-linear static simulation. The same applies for the strain of intermediate deformation states at the virtual sensor positions employed in the shape sensing. The required mode shapes

Table 1
Parameters of the wing geometry.

Parameter	Value
Half span	5 m
Planform area	3 m^2
Aspect ratio	16.67
Sweep angle	29°

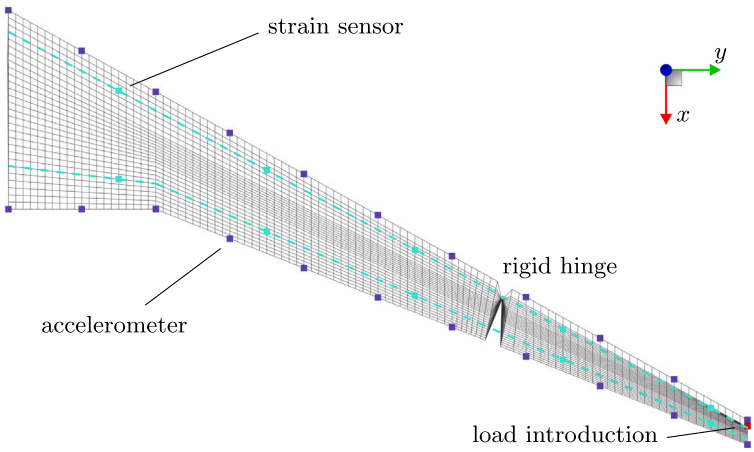

Fig. 2. Finite element grid of the wing with virtual sensor positions.

are obtained by normal modes analysis in these intermediate deformation states, taking into account geometric stiffness effects. For all simulations, the wing model is clamped at the root and, as indicated in the mesh plot, a tip load is introduced. The load introduction point at quarter chord is connected via rigid body constraints to all nodes of the tip cross-section. The load is applied as a dead load in the z-direction, not being affected of the deformation of the structure.

As mentioned in Section 2.2, the mode shapes are subjected to changes when the structure undergoes significant deformation. While the participation (modal coordinate) of each mode to the deformation reconstruction varies from increment to increment as well, across the deformation range considered, the first flapwise bending mode is the primary contributor in the described load case. Fig. 3 shows the displacement mode shape at various deformation states for the virtual instrumentation setup, expressed in global coordinates. As indicated in Figs. 3(b) and 3(c), increasing deformation amplitude results in larger spanwise components of the mode shape, which forms the basis for the spanwise shortening typically observed in geometrically nonlinear deformations of wing structures. Additionally, small in-plane components appear during deflection that are absent in the undeformed state due to the cross-sectional symmetry. By application of IMM, both the in-plane and spanwise components from intermediate deformation states induce displacements in their respective coordinate directions that are not present in the mode shape of the undeformed structure (Fig. 3(a)).

The illustrated setup describing the virtual sensor distribution and the particular load case is chosen because it represents a plausible structural test scenario, even though it is not physically representative of the pressure distribution typically associated with aerodynamic loading. This approach is deemed suitable, as the primary objective is to assess displacement reconstruction, with the specific cause of deformation being of secondary importance.

3.2. Reference results

Fig. 4 visualises the different components of the displacement field of the wing and the torsional deflection in the final deformation state. The tip is bent flapwise by 21.6%, shortened spanwise by 3.9%, and deflected edgewise by 1.3%, each relative to

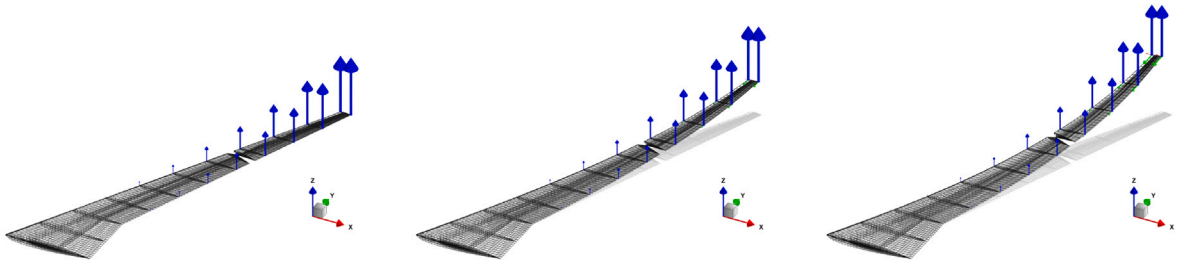

(a) undeformed structure (b) deformation at 50 % of target load (c) final deformation state

Fig. 3. 1st flapwise bending displacement mode shape at different deformation states.

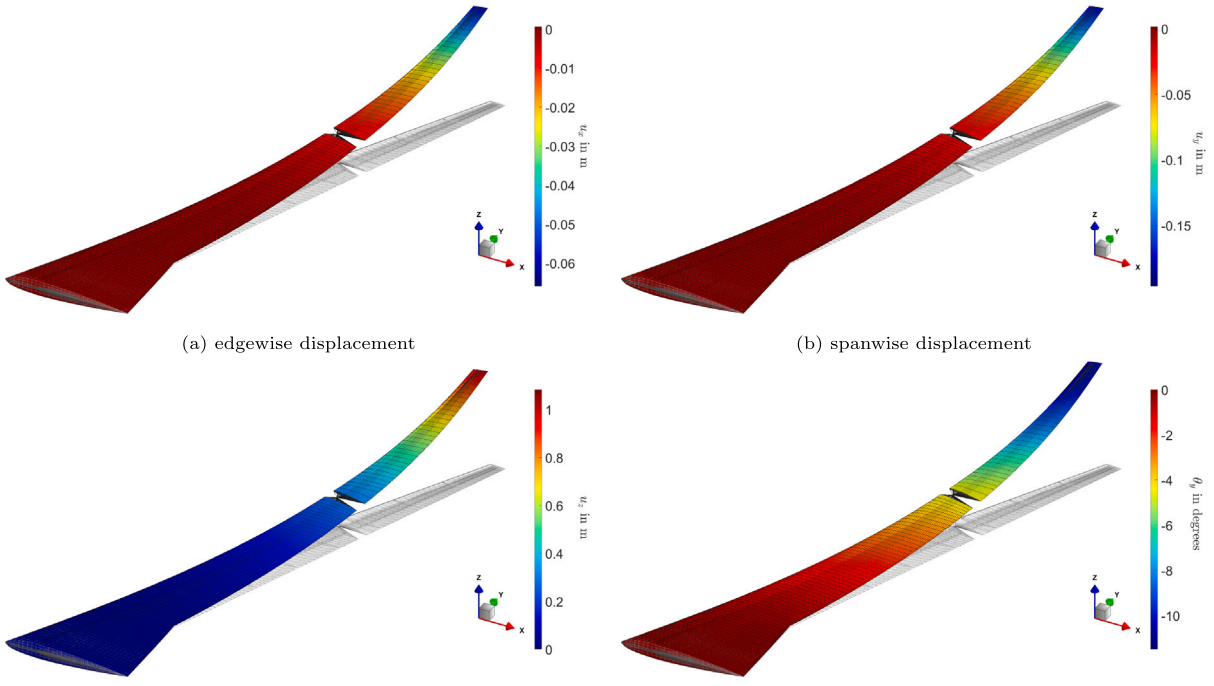

(a) edgewise displacement

(b) spanwise displacement

(c) flapwise displacement

(d) torsion deflection

Fig. 4. Displacement contour plots of non-linear target deformation state.

the original wing length. Based on the amount of flapwise bending and the shortening, the state of deformation clearly deviates from linear behaviour. Due to the sweep, the wing exhibits a tip twist of −11.2°, although a pure bending load is induced.

The deflection curves obtained using IMM with increments ranging from one to 16 are shown in Fig. 5. Fig. 5(a) displays the flapwise bending estimates $\hat{u}_z$ along the y-coordinate, normalised with respect to the original wing length. The diagrams also incorporate the spanwise displacements $\hat{u}_y$ that typically occur considering large deformation. The values are computed as arithmetic means of the estimates belonging to the nodes of the same cross-section. As a reference, the deflection curve obtained from non-linear FE analysis is plotted for comparison. The graphs reveal a convergence pattern, as the differences between the IMM solutions at the tip diminish with an increasing number of increments. Since the modal approach is applied based on a truncated set of only the ten lowest modes, the DST matrix does not span the full solution space of the FE model. As a result, the shape sensing

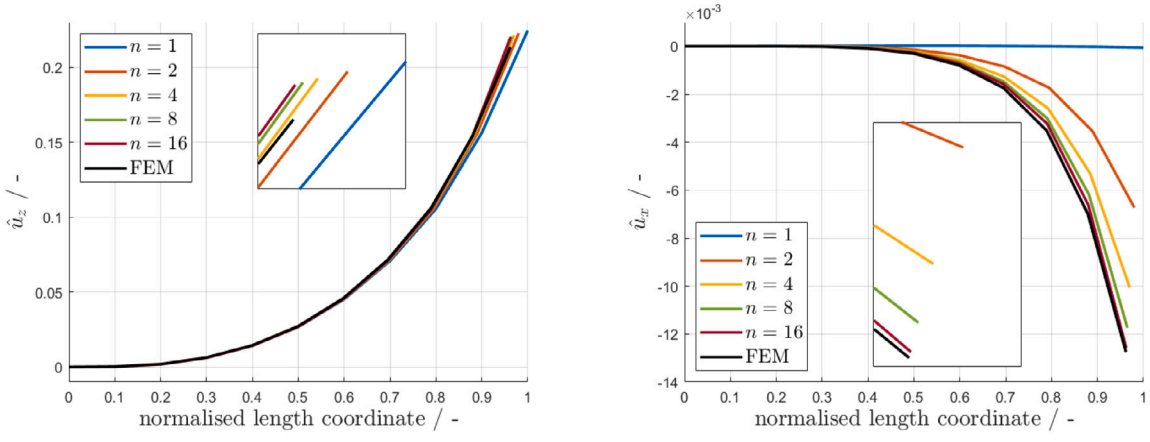

(a) flapwise bending estimates

(b) edgewise bending estimates

Fig. 5. Deterministic reconstruction results for varying number of increments.

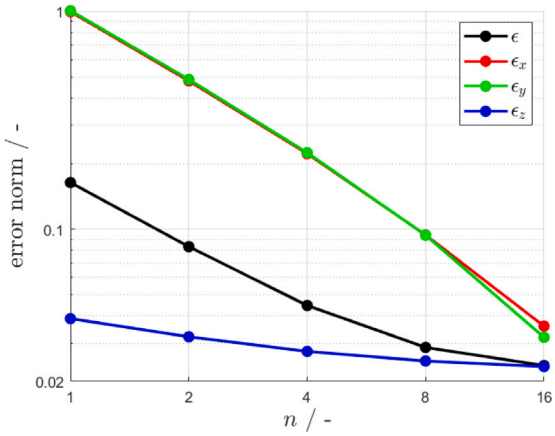

Fig. 6. Relative Euclidean error norm of the displacement estimates.

Table 2
Relative participation to overall deformation.

$\|\hat{u}_x\|/\|\hat{u}\|$	$\|\hat{u}_y\|/\|\hat{u}\|$	$\|\hat{u}_z\|/\|\hat{u}\|$
0.0500	0.1501	0.9874

solution does not fully converge to the reference results, even if the number of increments is further increased. Stronger convergence towards the reference solution can be observed regarding $\hat{u}_y$ and the edgewise displacements $\hat{u}_x$, as illustrated in Fig. 5(b), since these improvements are a direct result of capturing the non-linearity. It should be noted that using the modal shape sensing approach with a single increment ($n = 1$) does not account for significant displacements in these coordinate directions.

The error plots of Fig. 6 confirm the statements made about the reconstruction estimates. In the diagrams, the relative Euclidean norm of the error between the true displacements at virtual sensor locations and corresponding estimates is presented in logarithmic scale. The overall error norm is defined by:

$$\epsilon = \frac{\|\hat{\boldsymbol{u}} - \boldsymbol{u}\|}{\|\boldsymbol{u}\|}, \tag{25}$$

and the error quantities ϵ_x, ϵ_y, and ϵ_z pertain exclusively to displacements in the respective coordinate directions. As already mentioned, it is evident that applying IMM is most beneficial for the accuracy of estimates concerning the spanwise and edgewise direction, respectively; using $n = 8$ increments reduces the error of both displacements by an order of magnitude. The prediction of $\hat{u}_z$ also improves, with ϵ_z decreasing from 3.9% to 2.3% by incorporating the mode shapes of $n = 16$ deformation states on the path to the target deformation state. The error for the total deformation ϵ improves from 16.4% to 2.4% significantly better, although the deformation of the wing is dominated by flapwise bending, as indicated by the relative participation of the different displacement components (cf. Table 2).

Estimates $\hat{u}_z^{LE}$ and $\hat{u}_z^{TE}$, associated with the leading and trailing edges of the wing, respectively, can be utilised in shape sensing applications for approximation of the twist angle via (cf. [2,3])

$$\hat{\theta}_y = \arcsin\left(\frac{\hat{u}_z^{LE} - \hat{u}_z^{TE}}{\Delta x}\right), \tag{26}$$

where Δx specifies the chord length at these cross-sections. The results for varying number of increments are shown in Fig. 7 with the corresponding error plot. The illustrated error represents the relative norm defined in Eq. (25), calculated using the twist angle estimates $\hat{\boldsymbol{\theta}}_{\boldsymbol{y}}$ and references $\boldsymbol{\theta}_{\boldsymbol{y}}$, both obtained from the approximation in Eq. (26). The twist angles are derived from either displacement estimates or FE results at the leading and trailing edges, respectively. In addition to the FE reference line evaluated using Eq. (26), a dotted line representing the mean of the nodal rotations for the respective cross-sections is included for comparison. From the diagrams one observes that, opposing to all displacement estimates, a higher number of increments does not capture the twist angle more accurately.

From the deterministic results one can summarise that in principle, except for the twist angle, the IMM solutions exhibit a convergence trend for displacements to more accurate estimates as the number of increments increases. The following section examines whether, in addition to practical considerations of an experiment, there are implications from uncertainties with regard to the number of increments to be specified in the shape sensing.

4. Uncertainty analysis

The error propagation formulas derived in Section 2.3 can be used to analytically assess the influence of variability of the input quantities on the estimated displacement results. For this evaluation, the variability of the required mode shapes and the measured

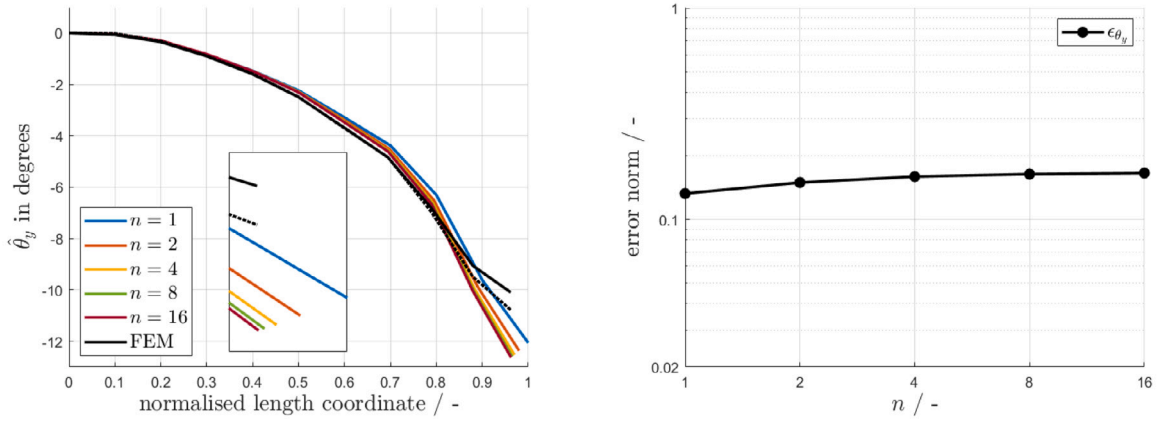

(a) torsional deflection estimates

(b) Relative Euclidean error norm of torsional deflection.

Fig. 7. Deterministic reconstruction results for varying number of increments.

strain in the relevant deformation states must be known. Monte Carlo simulations (MCS) are a widely used method in uncertainty quantification. They are commonly employed to assess the impact of uncertainties in various systems and models. Applying MCS in the scope of IMM, involves great effort if a larger number of increments is considered, as each displacement estimate of the MCS is the starting point for the MCS of the next increment. The number of analyses provided by the shape sensing method thus increases exponentially with the number of increments. The MCS approach has been employed in [35] for a linear shape sensing problem in an uncertainty quantification study comparing three different shape sensing methods with focus on material parameters and strain input uncertainty of an FE model, respectively. In the present research, MCS in combination with Latin Hypercube Sampling (LHS) [36] is used as a tool to verify the derived propagation laws. Therefore, the input parameters are sampled using UQLab [37] and the MCS is conducted in the MATLAB environment.

4.1. Uncertainty propagation from various input sources

The procedure described for checking the error propagation expressions in terms of Monte Carlo simulation is applied to the aforementioned sources of uncertainties. Basically, it is possible to consider the uncertainties for each individual measurement degree of freedom. However, the following section exemplarily examines the impact of uncertainties on the estimated displacements of the leading-edge wingtip sensor as a representative example.

4.1.1. Uncertainty arising from measured strain

Fig. 8 illustrates the propagation of uncertainties due to measured strain, as described by Eq. (10), for the estimates of the virtual leading-edge tip accelerometers over up to 16 increments. A significantly larger number of increments is not likely in the scope of an experiment. The strain input uncertainty of each strain signal is specified with $\sigma_\varepsilon = 5\mu\varepsilon$ for this case. In Fig. 8(a), the uncertainty trends are expressed in terms of the unscaled standard deviations. As expected, the increase of the output uncertainty is proportional to the square root of increments. This finding is supported by the least-squares fits of the type

$$\sigma^{\varepsilon}_{\hat{u}_j}(n) = k^{\varepsilon}\sqrt{n}, \tag{27}$$

which are shown as dotted lines. It should be mentioned that the uncertainties of the x- and y-coordinate are fitted more accurately with respect to $\sigma^{\varepsilon}_{\hat{u}_j}(n) = k^{\varepsilon}_1\sqrt{n + k^{\varepsilon}_2}$, which however involves a second constant in order to account for the offset on the abscissa.

From the diagram, one can tell that the uncertainties in edgewise wing direction are particularly high, knowing that edgewise displacements are of minor role in the overall deformation (cf. Fig. 4, Table 2). This is confirmed in Fig. 8(b), where the curves describe the relative standard deviation

$$\overline{\sigma}^{\varepsilon}_{\hat{u}^n_j} = \frac{\sigma^{\varepsilon}_{\hat{u}^n_j}}{|\mu^n_j|}, \tag{28}$$

where μ^n_j represent the deterministic estimates using n increments in the shape sensing; $\overline{\sigma}^{\varepsilon}_{\hat{u}^n_j}$ can be interpreted as the coefficient of variation of the displacement output. The relative measures indicate that for $n \geq 2$ the uncertainty for displacements in y-direction is lower compared to flapwise bending deflections. As the estimate for $n = 1$ does not bring about significant spanwise deformation (cf. Fig. 5(a)), the relative uncertainty is very high for using only a single increment. This also holds for the relative uncertainty of displacement estimates in x-direction, exhibiting qualitatively the same behaviour, but in the range of $3\% - 7\%$ for $n \in [2, 16]$.

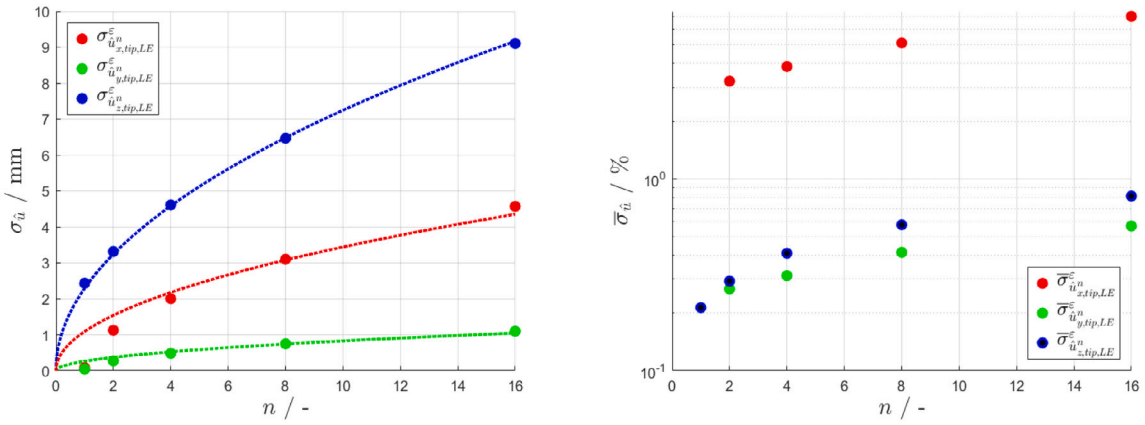

(a) Absolute standard deviation with least-squares fits (b) Relative standard deviation

Fig. 8. Uncertainty propagation from variable strain measurements for varying number of increments at the leading-edge wingtip.

In order to validate the propagation law, Monte Carlo simulations were conducted for one and two consecutive increments for displacements in the z-direction. To enable a comparison among datasets, the same number of 10^6 samples was used in both cases. For $n = 1$, all samples were generated by means of LHS in a single step, whereas for $n = 2$, only 10^3 instances were sampled prior to each shape sensing step, leading to the same total number of displacement estimates. A single sample comprises either the total strain ($n = 1$) or the strain increments ($n = 2$) of the 20 virtual strain sensors. The resulting histograms with identical bin width are visualised in Fig. 9, indicating a Gaussian distribution as probability density function for both discrete distributions. Due to the linearity of the transformation (cf. Eq. (6)), normally distributed σ_ε results in normally distributed displacement estimates. For the sake of comparison, Table 3 lists the deviation of the MCS results from the deterministic displacement estimates as well as from the analytical uncertainty values. These deviations are defined as

$$\begin{aligned} \Delta\hat{u}^n_{z,tip,LE} &= |\hat{u}^n_{z,tip,LE} - \mu_{\hat{u}^n}| \\ \Delta\sigma_{\hat{u}^n_{z,tip,LE}} &= |\sigma_{\hat{u}^n_{z,tip,LE}} - \sigma_{\hat{u}^n}|, \end{aligned} \tag{29}$$

where $\mu_{\hat{u}^n}$ and $\sigma_{\hat{u}^n}$ denote the mean and standard deviation of the corresponding frequency distribution, respectively.

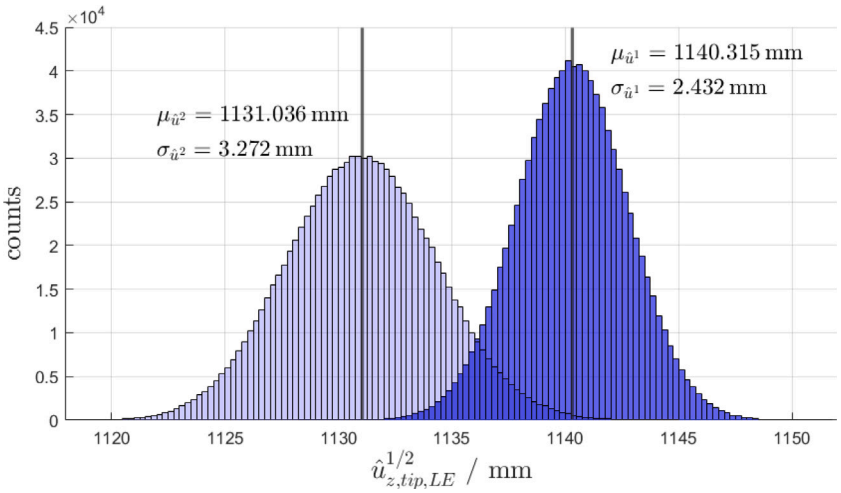

Fig. 9. Frequency distribution of displacement estimates using $n = 1$ and $n = 2$ increments from 10^6 strain samples with $\sigma_\varepsilon = 5\mu\varepsilon$.

It is observed that after two increments, the distribution becomes flatter and wider due to the increased uncertainty, compared to using only a single increment. As the non-linearity is taken into account with $n = 2$, the mean value improves towards the reference result of approximately $u_{z,tip,LE} = 1081$ mm. Regarding the mean and standard deviation values, the mean aligns with the deterministic solution, while the standard deviation shows a larger discrepancy from the analytical result using two increments. The

Table 3
Deviation from deterministic shape sensing estimates and from analytical uncertainties in %.

n	$\Delta\hat{u}^n_{z,tip,LE}$	$\Delta\sigma_{\hat{u}^n_{z,tip,LE}}$
1	$6.46 \cdot 10^{-6}$	0.02
2	$2.07 \cdot 10^{-4}$	1.28

latter can be explained by the fact that far fewer samples are used within an increment; an increase in the number of samples per increment would produce higher agreement of the uncertainties, but is associated with considerable costs.

This case demonstrates that the Gaussian propagation law in Eq. (10) can be applied as a replacement of costly MCS. It is also evident from the overlap of the distributions that due to more increments, increased measurement uncertainty may degrade the accuracy of the result, although a higher number of increments generally improves the deterministic estimate.

4.1.2. Uncertainty arising from displacement mode shapes

The uncertainties from displacement mode shapes are analysed in the same way as from measured strain. Here, a coefficient of variation of $c_v^{\Phi} = 0.01$ for each component of the displacement modal matrix is used, exemplifying the trend of the output uncertainties. The graphs describing the dependency on the number of increments in the shape sensing according to Eq. (17) are shown in Fig. 10(a). Again, the trends can be described by regression lines that are provided as dotted curves fitted with respect to

$$\sigma^{\Phi}_{\hat{u}_j}(n) = \frac{k^{\Phi}}{\sqrt{n}}, \tag{30}$$

following the relation found in Eq. (18). For the uncertainties of the displacements in x- and y-direction, the values at $n = 1$ are left out in the fitting, as they are not representable in above function, and using one increment only is not conceivable for non-linear problems. In contrast to uncertainties caused by strain, the relative standard deviation displayed in Fig. 10(b) is similar among all coordinate directions. A common feature of both cases is that the curves of the relative standard deviation for $n \in [2, 16]$ qualitatively follow the absolute standard deviation; for uncertainty in the displacement mode shapes, they are however all on the same level.

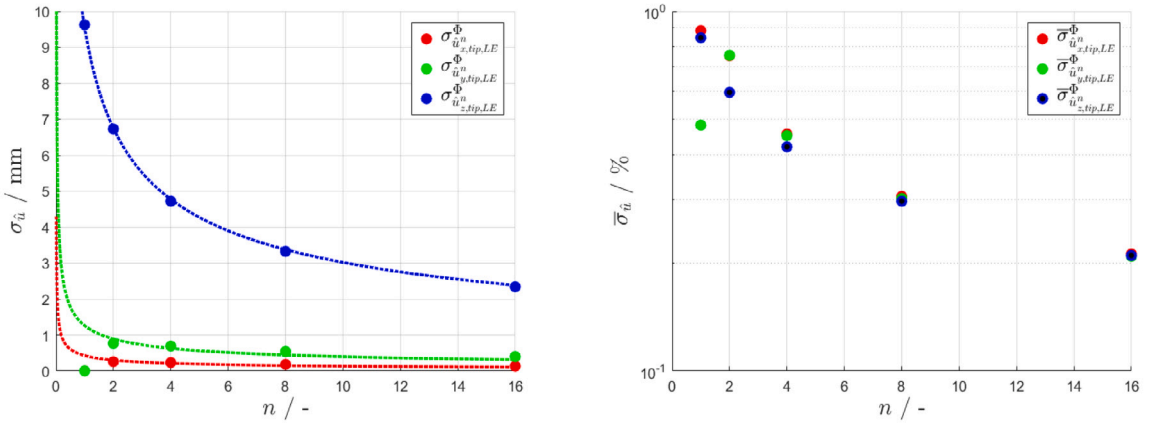

(a) Absolute standard deviation with least-squares fits (b) Relative standard deviation

Fig. 10. Uncertainty propagation from variable displacement mode shapes for varying number of increments at the leading-edge wingtip.

Again, MCS are conducted for the z-direction DOF to verify the propagation formula. This time, all components of the displacement modal matrix undergo a normally distributed random sampling with $c_v^{\Phi} = 0.01$. Using ten modes, a single sample matrix comprises 660 entries that are set with LHS. For the single step MCS, all 10^6 instances are sampled at once, whereas for two increments only 10^3 samples are created for each increment. The results of the MCS are illustrated in the histograms of Fig. 11 with the percentual deviation from the deterministic mean and from analytical values of the standard deviations (cf. Eq. (29)) shown in Table 4. The mapping from strain to displacements is linear in terms of mode shape components; therefore, the frequency distribution

Table 4
Deviation from deterministic shape sensing estimates and from analytical uncertainties in %.

n	$\Delta\hat{u}^n_{z,tip,LE}$	$\Delta\sigma_{\hat{u}^n_{z,tip,LE}}$
1	$4.51 \cdot 10^{-6}$	$3.01 \cdot 10^{-3}$
2	$3.20 \cdot 10^{-4}$	0.18

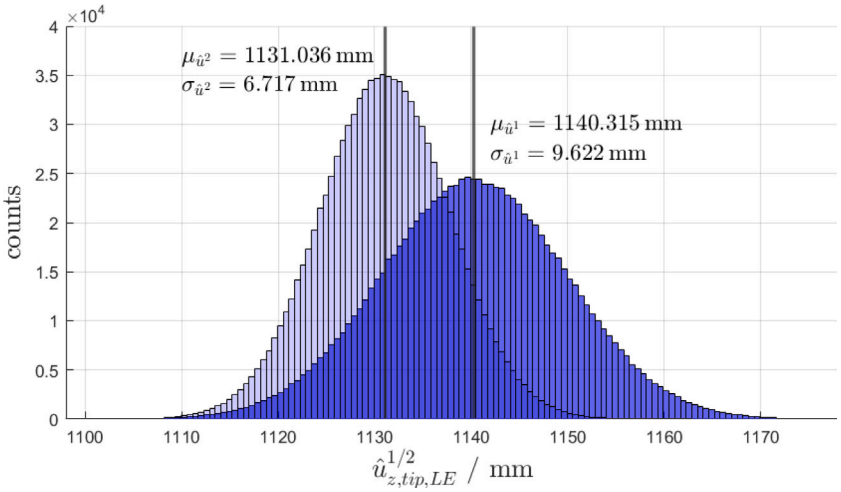

Fig. 11. Frequency distribution of displacement estimates using $n = 1$ and $n = 2$ increments from 10^6 sampled displacement modal matrices and $c_v^{\Phi} = 0.01$.

of the displacements closely follows a normal distribution. As expected, solving the problem in a single step not only results in a less accurate mean value but also yields a higher standard deviation compared to the incremental approach. The mean values consistently predict well the deterministic estimates (cf. Table 3), and once again the analytical values of the standard deviation are better met with $n = 1$ for the larger number of samples. In total, it can be stated that the propagation of uncertainties from displacement mode shapes can be described by the expression presented in Eq. (17).

4.1.3. Uncertainty arising from strain mode shapes

Finally, the uncertainties resulting from the variability of the strain mode shapes are analysed. Deriving the propagation law is more complex, as the strain mode shapes are processed in a pseudoinverse within the shape sensing method. Analogous to the displacement modes, a coefficient of variation of $c_v^{\Psi} = 0.01$ is assumed to exemplify the uncertainty quantification. As with the other input variables, this can be changed as desired, the trends remain unchanged, only the magnitude of the resulting uncertainty on the estimated displacements depends linearly on the coefficient of variation.

Fig. 12(a) shows the evolution of the uncertainties for the various displacement components with their associated regression curves. As previously with the displacement modes, the least-squares fits are performed with a function of the same type

$$\sigma^{\Psi}_{\hat{u}_j}(n) = \frac{k^{\Psi}}{\sqrt{n}}, \tag{31}$$

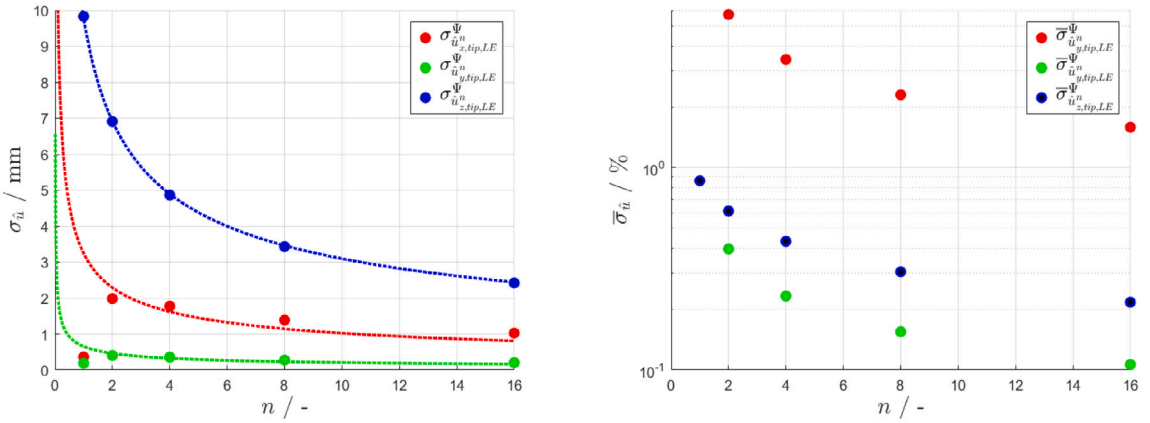

(a) Absolute standard deviation with least-squares fits

(b) Relative standard deviation

Fig. 12. Uncertainty propagation from variable strain mode shapes for varying number of increments at the leading-edge wingtip.

whereby $n = 1$ was omitted for the x- and y-coordinate. For coefficients of variation of the same size, the results are qualitatively and also quantitatively similar to the uncertainties for displacement modes. The uncertainties for displacements in the edgewise direction are an exception: they are clearly excessive, as in the case of uncertainties in the strain measurements. This is confirmed by the relative standard deviation shown in Fig. 12(b). The uncertainties for the x-direction displacements fall outside the displayed range but follow a similar trend to the other two displacement components within $n \in [2, 16]$, with a relative standard deviation between 6% and 2%. When looking at the relative standard deviation from all input variables, it can be seen that in all three cases the relative uncertainty follows the trend of the absolute uncertainties.

The propagation formula in Eq. (23) is checked in the same way as in the previous two cases. With 10 modes considered in shape sensing, each sample of the strain modal matrix encompasses a total of 200 components. The same total number of samples is used for the MCS as in the previous examples and the results are depicted in Fig. 13 with the deviation from the deterministic estimates and from analytical values of the standard deviation listed in Table 5. The histograms resemble to those illustrated for the displacement mode shapes, as the propagation for both types of mode shape uncertainties has a similar functional dependency.

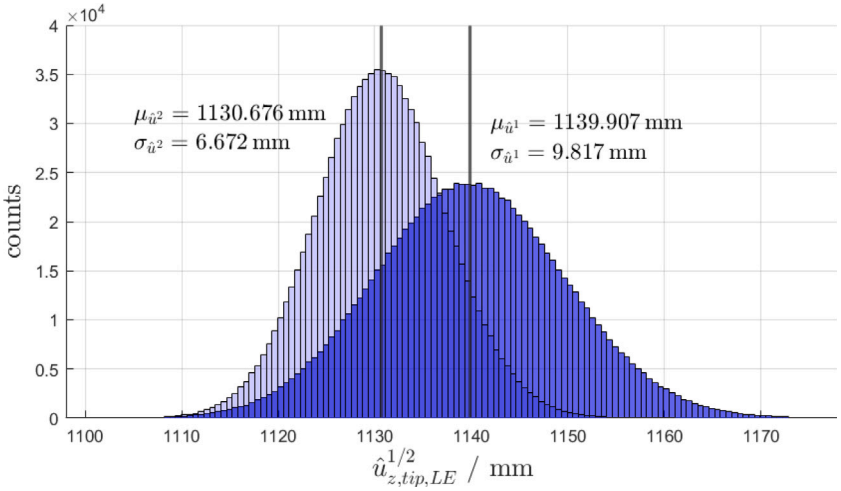

Fig. 13. Probability density functions using $n = 1$ and $n = 2$ increments from 10^6 strain modal matrices and $c_v^{\Psi} = 0.01$.

Table 5
Deviation from deterministic shape sensing estimates and from analytical uncertainties in %.

n	$\Delta\hat{u}^n_{z,tip,LE}$	$\Delta\sigma_{\hat{u}^n_{z,tip,LE}}$
1	0.04	0.13
2	0.03	3.43

Unlike the other two cases, this result exhibits significant deviation between the mean values of the MCS results and the deterministic displacement estimates. Additionally, an increase of the discrepancies between standard deviations from MCS and analytical standard deviations can be observed. Both effects can be attributed to the fact that the Gauss formula provides only a linear approximation of the actual uncertainty propagation when dealing with uncertainties from strain modes. Fig. 14 illustrates how the error in standard deviation, defined as

$$\epsilon_\sigma = \frac{\sigma^{\Psi}_{Gauss} - \sigma^{\Psi}_{MCS}}{\sigma^{\Psi}_{MCS}}, \tag{32}$$

manifests for varying coefficients of variation in the case of a single increment. The diagrams consider all components of displacement at the leading-edge wingtip position. By means of above definition, one can observe from the error plot that the analytical formula overestimates the standard deviation of estimates concerning displacements in all coordinate directions. Significant differences evolve above $c_v^{\Psi} = 0.01$, and the error is in general larger for the flapwise displacement. If the systematically overestimated uncertainties are propagated over several increments, the output in these increments will also overestimate the uncertainty due to a chain effect. Using Eq. (23) is thus conservative with regard to the standard deviation.

The non-linearity in strain modes also causes the disagreement between the mean of the histograms and the deterministic displacement estimates of the shape sensing. As depicted in Fig. 15, the frequency distribution of the MCS are affected by a skew to lower displacement estimates, which becomes more apparent with increasing c_v^{Ψ}. For this reason, the mean value from the MCS is also lower compared to the displacement estimate without uncertainties. This effect cannot be accurately captured by using the propagation law. However, with low variability of the strain modes, it provides a sound approximation for the uncertainty propagation behaviour of the incremental shape sensing method.

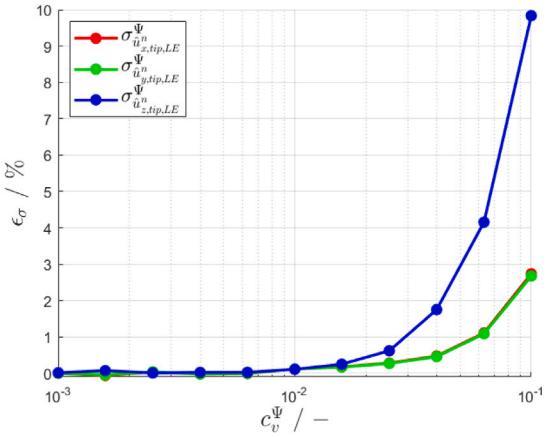

Fig. 14. Discrepancy between analytical propagation and MCS for $n = 1$.

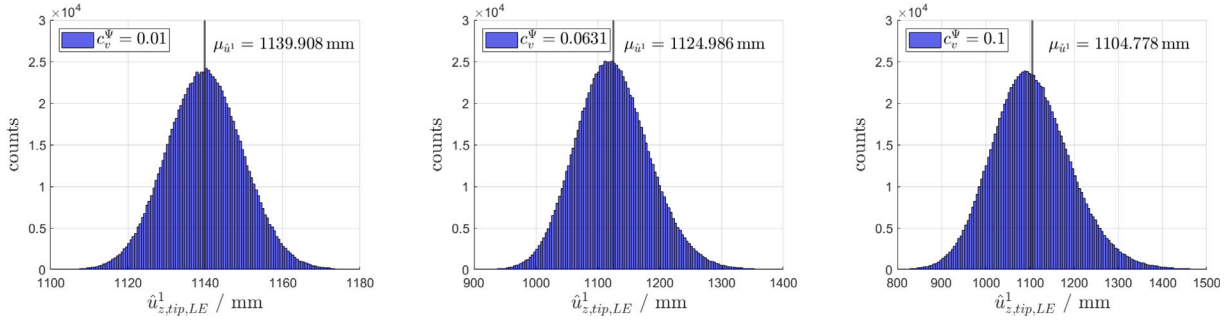

Fig. 15. Histograms of displacement output from MCS with a single increment accounting for variable strain mode shapes. The PDFs exhibit notable skew for increased c_v^{Ψ}.

4.2. Overall uncertainty quantification

Since the propagation of individual sources of uncertainty is accurately captured, the overall uncertainty, as determined by the deformation at the leading-edge wingtip, is analysed in the following section. Assuming that the input quantities are independent, the sum rule of variances applies for the different uncertainties. By using the fitting functions, one obtains the total uncertainty

$$\sigma^{\Sigma}_{\hat{u}_j}(n) = \sqrt{k^{\varepsilon\,2} n + \frac{k^{\Phi\,2} + k^{\Psi\,2}}{n}}, \tag{33}$$

which exhibits a minimum at

$$n_{min} = \sqrt{\frac{k^{\Phi\,2} + k^{\Psi\,2}}{k^{\varepsilon\,2}}}. \tag{34}$$

The exemplified cases of the different input parameters of the shape sensing ($\sigma_\varepsilon = 5\mu\varepsilon$, $c_v^{\Phi} = 0.01$, $c_v^{\Psi} = 0.01$) lead to the fitted parameters in Table 6. These bring about optimal choices of n_{min}, where the overall uncertainty of the different displacement directions at the leading-edge wingtip would be the smallest. The corresponding plots are displayed in Fig. 16. The three curves have in common that they decrease until the uncertainty stemming from measured strain prevails. As the deformation is dominated by the displacements in y- and z-direction, respectively, a good choice to minimise the uncertainty would be either $n = 5$ or $n = 6$.

Table 6
Parameters of the fitting functions.

	k^{ε}	k^{Φ}	k^{Ψ}	n_{min}
u_x	1.0882	0.4295	3.2435	3.00
u_y	0.2614	1.2624	0.6555	5.44
u_z	2.2914	9.5494	9.7896	5.97

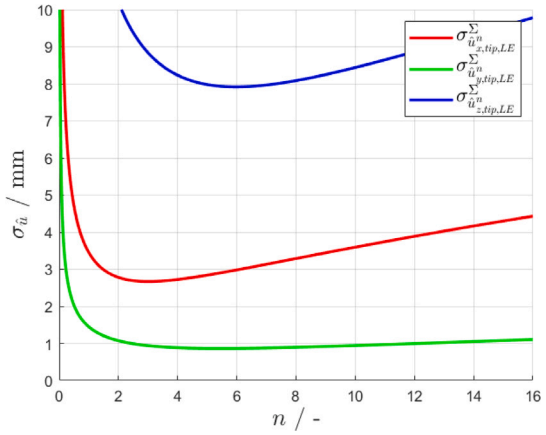

Fig. 16. Overall uncertainty plots.

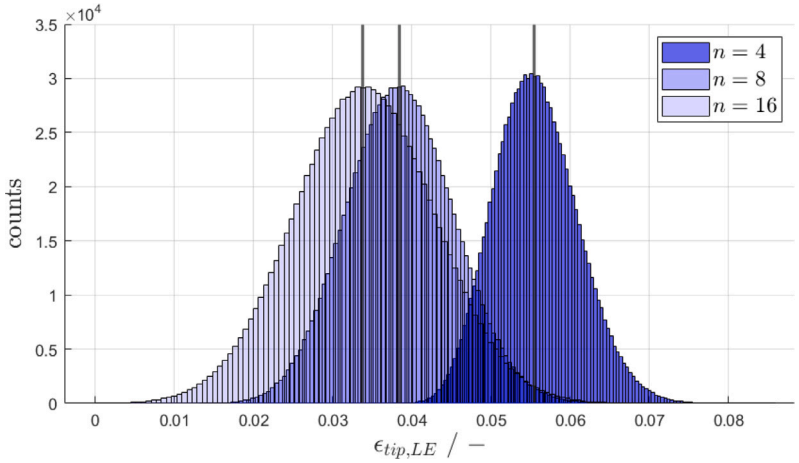

Fig. 17. Histograms of displacement estimate for the leading-edge wingtip including input uncertainties from strain measurements and mode shapes.

In most cases, one is rather interested to maximise the accuracy of the shape sensing in a specific application. It is not only impractical to consider huge amounts of increments to obtain the displacements in a geometrically non-linear deformation state, moreover do the uncertainties increase monotonously. Therefore, it is essential to verify whether a more refined representation of the non-linearity, achieved through additional increments, is justified in light of the uncertainties. For the high-aspect-ratio wing, this issue is deliberated with the help of Fig. 17.

It shows the relative Euclidean norm (cf. Eq. (25)) of the error at the leading-edge wingtip using either 4, 8 or 16 increments. The displacement vectors used for the histograms were derived from the deterministic estimates, indicated by vertical lines, and through random sampling of the uncertainties associated with individual displacement vector components at the corresponding number of increments. While $n = 4$ increments clearly leads to more inaccurate results, the transition from $n = 8$ to $n = 16$ increments is not necessarily justified. First, the deterministic estimates do not improve to the same extent and second, the increased uncertainty leads to a wider spectrum of possible error. On that account, approximately 30% of the results using 16 increments yield a higher error than the mean error of using 8 increments. Moreover, due to uncertainties, there is a small probability (less than 1%) that an estimate with 16 increments could be worse than all possible outcomes achievable with 8 increments.

5. Conclusions

This paper introduces the incremental modal shape sensing method for geometrically nonlinear problems and presents an analytical approach to uncertainty propagation within this framework, utilising Gaussian error propagation. The shape sensing method has been applied on numerical data obtained with an FE model of a high-aspect-ratio wing at virtual sensor positions. Deterministic shape sensing exhibits the convergence behaviour of the method. In combination with the deterministic estimates, the impact of different sources of uncertainty can be described and evaluated for different number of increments.

For deterministic shape sensing, the wing was analysed in a non-linear bending deformation state. The results revealed that increasing the number of increments improves the accuracy of displacement estimates with respect to the finite element solution. Particularly, spanwise and edgewise displacements improve when the incremental modal method is applied. An exception is the twist angle derived from out-of-plane displacements at leading and trailing edges, which shows no improvement with more increments possibly due to the simplified evaluation approach.

In the uncertainty quantification analysis, it was found that within the interval of 2 to 16 increments, the uncertainties of the primary input sources — measured strain, displacement mode shapes, and strain mode shapes — can be effectively modelled using simple root functions. It was evident that the uncertainties from measured strain increase proportionally to the square root of the increments, while the uncertainties from mode shapes both decrease inversely with the same relationship. Results from Monte Carlo simulations confirm the Gaussian uncertainty propagation formulas as a cost-effective alternative to extensive simulations. Furthermore, the analytical expressions enable the optimisation of the testing strategy concerning output uncertainty. Since strain mode shapes are non-linearly transformed into displacements in the shape sensing, the analytical propagation law is only an approximation; depending on the variability of the mode shapes, the uncertainties are slightly overestimated. The combined uncertainty analysis indicates that beyond a certain number of increments, uncertainties can outweigh the benefits of improved deterministic accuracy.

In principle, the analysis of uncertainties as presented here can generally be employed in shape sensing applications using the incremental modal method, for instance in wind tunnel or structural dynamic test scenarios. The illustrated procedure is applicable regardless of the sensor distribution on the test specimen or the number of available modes. Uncertainties of the modal method for linear methods problems are already included as a special case with one increment. The prerequisite is that the corresponding uncertainties in the different deformation states can be expressed as standard deviations (variances) of a normally distributed probability density function. From a practical perspective, meeting this requirement is likely more straightforward for the measured strains than for the mode shapes.

Determining the optimal number of increments for accuracy requires an adequately updated FE model. Then, the process could also be carried out for fitting functions that describe the course of the standard deviations over the number of increments more accurately, for arbitrary ranges of increments. Furthermore, the determination of the optimal number of increments could be addressed in an optimisation scheme that, for instance, favours the accuracy at specific locations on the wing. In this way, the method presented here can contribute to the effective application of the shape-sensing approach in the framework of a complex measurement task in the geometrically non-linear domain.

CRediT authorship contribution statement

Janto Gundlach: Writing – original draft, Visualization, Software, Methodology, Formal analysis, Conceptualization. **Marc Böswald:** Writing – review & editing, Supervision, Funding acquisition, Conceptualization. **Jurij Sodja:** Writing – review & editing, Supervision, Conceptualization.

Declaration of competing interest

The authors declare that they have no known competing financial interests or personal relationships that could have appeared to influence the work reported in this paper.

Acknowledgements

This work is part of the DLR project ACTIVATE and the MuStHaF project which is financed by the Federal Ministry of Economic Affairs and Climate Action (BMWK) grant agreement ID 20A2103C.

Supported by:

Federal Ministry
for Economic Affairs
and Climate Action

on the basis of a decision
by the German Bundestag

Data availability

The data that has been used is confidential.

References

[1] M. Gherlone, P. Cerracchio, M. Mattone, Shape sensing methods: Review and experimental comparison on a wing-shaped plate, Prog. Aerosp. Sci. 99 (2018) 14–26, http://dx.doi.org/10.1016/j.paerosci.2018.04.001.

[2] W.L. Ko, W.L. Richards, V.T. Tran, Displacement Theories for In-Flight Deformed Shape and Predictions of Aerospace Structures, Tech. Rep. NASA/TP-2007-214612, NASA Dryden Flight Research Center, Edwards, California, 2007, URL https://ntrs.nasa.gov/citations/20070032936.

[3] W.L. Ko, V.T. Fleischer, Further Development of Ko Displacement Theory for Deformed Shape Predictions of Nonuniform Aerospace Structures, Tech. Rep. NASA/TP-2009-214643, NASA Dryden Flight Research Center, Edwards, California, 2009, URL https://ntrs.nasa.gov/citations/20090034086.

[4] A. Tessler, J.L. Spangler, A least-squares variational method for full-field reconstruction of elastic deformations in shear-deformable plates and shells, Comput. Methods Appl. Mech. Engrg. 194 (2–5) (2005) 327–339, http://dx.doi.org/10.1016/j.cma.2004.03.015.

[5] G.C. Foss, E.D. Haugse, Using modal test results to develop strain to displacement transformations, in: Proceedings of the IMAC XIII, Society for Experimental Mechanics (SEM), Nashville, Tennessee, USA, 1995.

[6] M.A. Davis, A.D. Kersay, J. Sirkis, E.J. Friebele, Shape and vibration mode sensing using a fiber optic Bragg and grating array, Smart Mater. Struct. 5 (1996) 759–765.

[7] P. Bogert, E. Haugse, R.E. Gehrki, Structural shape identification from experimental strains using a modal transformation technique, in: 44th AIAA/ASME/ASCE/AHS/ASC Structures, Structural Dynamics, and Materials Conference, no. Technology, American Institute of Aeronautics and Astronautics, 2003, http://dx.doi.org/10.2514/6.2003-1626.

[8] A. Drachinsky, D.E. Raveh, Modal rotations: A modal-based method for large structural deformations of slender bodies, AIAA J. 58 (7) (2020) 3159–3173, http://dx.doi.org/10.2514/1.j058899.

[9] A. Drachinsky, D.E. Raveh, Nonlinear aeroelastic analysis of highly flexible wings using the modal rotation method, AIAA J. 60 (5) (2022) 3122–3134, http://dx.doi.org/10.2514/1.j061065.

[10] C.-G. Pak, Linear and geometrically nonlinear structural shape sensing from strain data, AIAA J. 61 (2) (2023) http://dx.doi.org/10.2514/1.J062165.

[11] C.-G. Pak, Wing shape sensing from measured strain, AIAA J. 54 (3) (2016) 1068–1077, http://dx.doi.org/10.2514/1.j053986.

[12] A. Tessler, R. Roy, M. Esposito, C. Surace, M. Gherlone, Shape sensing of plate and shell structures undergoing large displacements using the inverse finite element method, Shock. Vib. (2018) http://dx.doi.org/10.1155/2018/8076085.

[13] M. Li, D. Jia, H. Huang, W. Ziyan, A. Kefal, Geometrically nonlinear deformation reconstruction based on iQS4 elements using a linearized iterative iFEM algorithm, Acta Mech. Solida Sin. 36 (2023) 166–180, http://dx.doi.org/10.1007/s10338-022-00369-6.

[14] M. Böswald, Y. Govers, G. Jelicic, R. Buchbach, Online monitoring of flutter stability during wind tunnel testing of an elastic wing with pylon and engine nacelle within the HMAE1 project, 2019, URL https://elib.dlr.de/128030/.

[15] G. Jelicic, J. Schwochow, Y. Govers, J. Sinske, R. Buchbach, J. Springer, Online monitoring of aircraft modal parameters during flight test based on permanent output-only modal analysis, 2017, http://dx.doi.org/10.2514/6.2017-1825.

[16] R. Volkmar, K. Soal, Y. Govers, M. Böswald, Experimental and operational modal analysis: Automated system identification for safety-critical applications, Mech. Syst. Signal Process. 183 (2023) 109658, http://dx.doi.org/10.1016/j.ymssp.2022.109658.

[17] F. Magalhães, Á. Cunha, E. Caetano, Online automatic identification of the modal parameters of a long span arch bridge, Mech. Syst. Signal Process. 23 (2009) 316–329, http://dx.doi.org/10.1016/j.ymssp.2008.05.003.

[18] J. Gundlach, M. Böswald, J. Sofja, An Incremental Modal Shape Sensing Method for Geometrically Non-Linear Deformed Wings, The Hague, The Netherlands, 2024, URL https://elib.dlr.de/207213/.

[19] A. Brandt, Noise and Vibration Analysis, second ed., John Wiley and Sons, 2023, http://dx.doi.org/10.1002/9781118962176.

[20] R. Brincker, C.E. Ventura, Introduction to Operational Modal Analysis, Wiley & Sons, Ltd, 2015, http://dx.doi.org/10.1002/9781118535141.

[21] O. Bernasconi, D. Ewins, Application of strain modal testing to real structures, in: Proceedings of the 7th International Modal Analysis Conference, Society for Experimental Mechanics (SEM), Las Vegas, Nevada, 1989.

[22] L.H. Yam, T.P. Leung, D.B. Li, K.Z. Xue, Theoretical and experimental study of modal strain analysis, J. Sound Vib. 191 (2) (1996) 251–260, http://dx.doi.org/10.1006/jsvi.1996.0119.

[23] T. Kranjc, J. Slavič, M. Boltežar, A comparison of the strain and the classic experimental modal analysis, J. Vib. Control (2014) http://dx.doi.org/10.1177/1077546314533137.

[24] L.-H. Kang, D.-K. Kim, J.-H. Han, Estimation of dynamic structural displacements using fiber Bragg grating strain sensors, J. Sound Vib. 305 (2007) 534–542, http://dx.doi.org/10.1016/j.jsv.2007.04.037.

[25] S. Rapp, L.-H. Kang, J.-H. Han, U.C. Mueller, H. Baier, Displacement field estimation for a two-dimensional structure using fiber Bragg grating sensors, Smart Marterials Struct. 18 (025006) (2009) http://dx.doi.org/10.1088/0964-1726/18/2/025006.

[26] H.-I. Kim, L.-H. Kang, J.-H. Han, Shape estimation with distributed fiber Bragg grating sensors for rotating structures, Smart Mater. Struct. 20 (035011) (2011) http://dx.doi.org/10.1088/0964-1726/20/3/035011.

[27] H.-I. Kim, J.-H. Han, H.-J. Bang, Real-time deformed shape estimation of a wind turbine blade using distributed fiber Bragg grating sensors, Wind. Energy 17 (2014) 1455–1467, http://dx.doi.org/10.1002/we.1644.

[28] M.I. Friswell, J.E. Mottershead, in: G.M.L. Gladwell (Ed.), Finite Element Model Updating in Structural Dynamics, in: Solid Mechanics and its Applications, Springer Science and Business Media, B.V., 1996, http://dx.doi.org/10.1007/978-94-015-8508-8.

[29] R.J. Allemang, The modal assurance criterion – twenty years of use and abuse, Sound Vib. (2003) 14–20, URL http://www.sandv.com/downloads/0308alle.pdf.

[30] H.H. Ku, Notes on the use of propagation of error formulas, J. Res. Natl. Bur. Stand. 70C (4) (1966) http://dx.doi.org/10.6028/jres.070c.025.

[31] M. Loève, in: F.W. Gehring (Ed.), fourth ed., Probability Theory I, vol. 1, Springer New York Heidelberg Berlin, 1977, http://dx.doi.org/10.1007/978-1-4684-9464-8.

[32] E.N. Jacobs, K.E. Ward, R.M. Pinkerton, The Characteristics of 78 Related Airfoil Sections from Tests in the Variable-Density Wind Tunnel, Tech. Rep. 460, National Advisory Committee for Aeronautics (NASA), Washington, DC, USA, 1933, URL https://ntrs.nasa.gov/citations/19930091108.

[33] T. Klimmek, Parameterization of topology and geometry for the multidisciplinary optimization of wing structures, in: Proceedings of the European Air and Space Conference 2009, 2009, URL https://elib.dlr.de/65746/.

[34] M. Schmücker, LTH - Aeronautical Engineering Handbook: Calibration of Main Components of an Aircraft for Loads, LTH Executive Secretary, Ottobrunn, 2010.

[35] M. Esposito, M. Gherlone, Material and strain sensing uncertainties quantification for the shape sensing of a composite wing box, Mech. Syst. Signal Process. 160 (107875) (2021) http://dx.doi.org/10.1016/j.ymssp.2021.107875.

[36] C.P. Robert, G. Casella, Monte Carlo Statistical Methods, second ed., in: Springer Texts in Statistics, Springer Science+Business Media New York, 2004, http://dx.doi.org/10.1007/978-1-4757-4145-2.

[37] S. Marelli, B. Sudret, UQLab: A framework for uncertainty quantification in MATLAB, in: The 2nd Internation Conference on Vulnerability and Risk Analysis and Management, ICVRAM 2014, 2014, http://dx.doi.org/10.1061/9780784413609.257.